Single-Atom Manganese-Based Catalysts for the Oxidative Dehydrogenation of Propane

Journal:	*ACS Catalysis*
Manuscript ID	cs-2024-06021y
Manuscript Type:	Article
Date Submitted by the Author:	30-Sep-2024

Complete List of Authors:	Byron, Carly; Argonne National Laboratory, Chemical Sciences and Engineering Division Ignacio-de Leon , Patricia; Argonne National Laboratory, Advanced Materials Division Bryant, Jacob; Argonne National Laboratory, Chemical Sciences and Engineering Division Langeslay, Ryan; Argonne National Laboratory, Chemical Sciences and Engineering Division Savereide, Louisa; Northwestern University, Department of Chemical and Biological Engineering Wen, Jianguo; Argonne National Laboratory, Center for Nanoscale Materials Camacho-Bunquin, Jeffrey; Argonne National Laboratory, Chemical Sciences and Engineering Division Notestein, Justin; Northwestern University, Chemical and Biological Engineering Delferro, Massimiliano; Argonne National Laboratory, Chemical Sciences and Engineering Division Ferrandon, Magali; Argonne National Laboratory, Chemical Sciences and Engineering Division

Single-Atom Manganese-Based Catalysts for the Oxidative Dehydrogenation of Propane

Carly Byron,[a] Patricia Anne Ignacio-de Leon,[b] Jacob Bryant,[a] Ryan Langeslay,[a] Louisa Savereide,[c] Jianguo Wen,[d] Jeffrey Camacho-Bunquin,[a] Justin M. Notestein,[c] Massimiliano Delferro[*a] and Magali Ferrandon*[a]

[a] Chemical Sciences and Engineering Division, Argonne National Laboratory, Lemont, IL, USA 60439
[b] Advanced Materials Division, Argonne National Laboratory, 9700 South Cass Avenue, Lemont, IL, USA 60439
[c] Department of Chemical and Biological Engineering, Northwestern University, Evanston, IL, USA 60208
[d] Center for Nanoscale Materials, Argonne National Laboratory, Lemont, IL, USA 60439

KEYWORDS Propane dehydrogenation • single atom • manganese • vanadium • nickel • combinatorial screening

ABSTRACT: Combinatorial screening of 150 supported metal oxide (manganese and additives) catalysts was carried out via high-throughput synthesis platform and parallel reactors for the oxidative dehydrogenation (ODH) of propane to propylene. Specifically, an organomanganese (0.05 to 2.5 Mn atoms/nm^2) complex was grafted on metal oxide supports (Al_2O_3, SiO_2, TiO_2, and ZrO_2) pre-modified with either Lewis acid (Al, Ti, Zn and Zr) or redox-active (Cu, Cr, Ga Ni, V) additives at various surface coverages (25, 50 and 75%). Catalysts were characterized by high-resolution transmission electron microscope, X-ray photoelectron spectroscopy, X-ray diffraction, Raman spectroscopy, and UV-vis spectroscopy. Catalysts 0.05 Mn/V(50%)/Al_2O_3 and 0.05 Mn/Ni(50%)/ZrO_2 showed the highest combined propane conversion and propylene selectivities (31/41% and 15/85%), with excellent stability at 500 °C for 25 h. The presence of Ni in Mn/Ni/ZrO_2 resulted in a 6-fold increase in turnover frequency (TOF) over the Mn/ZrO_2. HRTEM identified single Mn atoms after 500 °C heat treatment. For Mn/Ni/ZrO_2 system, Mn was incorporated into the support lattice due to similar ionic radius of Mn^{2+} and Zr^{4+}, which was also enhanced by the presence of Ni. For Mn/V/Al_2O_3 system, highly active MnO was prevalent as observed by Raman. Both V and Mn contributed to an increase in mutual dispersion, but both species remained on the surface. It is proposed that the highly dispersed atom and interactions between Mn with either Ni or V are responsible for the ODH performance and stability.

Introduction

Propylene is the second largest-volume chemical produced globally. It is an important raw material for the production of commodity chemicals, in particular polypropylene.[1] Among all the synthesis routes, catalytic non-oxidative dehydrogenation (PDH, 1) is the most direct and selective way to produce propylene.[2] Commercially, the Catofin (Cr_2O_3/Al_2O_3) and Oleflex ($PtSn/Al_2O_3$) catalytic processes are widely used for propane dehydrogenation,[3] however, catalysts used in these processes suffer from sintering and coking due to typical reaction conditions employed at such high temperatures (> 500 °C) and the absence of oxygen.[4] In addition, the endothermicity of the reaction demands high energy input. Catalytic oxidative dehydrogenation (ODH, 2) of propane provides an alternative to PDH because of its exothermicity, lower reaction temperatures, and reduced coke deposition.[5,6]

PDH propane $C_3H_8 \leftrightarrow C_3H_6 + H_2$ (1)

ΔG_{25} = +86 kJ/mol

ODH propane $C_3H_8 + 1/2\ O_2 \leftrightarrow C_3H_6 + 2\ H_2O$ (2)

ΔG_{25} = -142 kJ/mol

However, since the desired olefin product is more reactive than the starting alkane, the challenge for the oxidative dehydrogenation is to limit the undesired side reactions resulting in CO_2 and CO formation. Factors such as temperature,[7] oxygen partial pressure,[8,9] reactor design[10] and catalyst compositions[5] have been shown to tune and minimize overoxidation.

Vanadium oxide- and molybdenum oxide-based catalysts are the most reported systems in the current literature for propane ODH.[5] Redox active metal oxides are usually more selective for the ODH of alkanes which follows a Mars-van Krevelen mechanism.[5] In addition, manganese-based catalysts exhibit interesting catalytic ODH performances and they have gained more attention over the past decades.[8–13] However, manganese-based catalysts are prone to form catalytic-inactive species under oxidative conditions due to agglomeration and sintering.[14]

One of the key components for the ODH reaction is the reducibility of the surface metal oxide species. It has been reported that the reducibility of manganese oxide depends on its dispersion which, in turn, is affected by several factors such as the metal loading, choice of the metal precursors, the support surface area, as well as its acid and basic nature.[5,11,15] Reducibility may also be enhanced by modifying oxide surfaces with a second more reducible oxide ($M'O_x$) that replaces the M-O-support linkages with more reactive M-O-M' linkages.[16,17] This beneficial effect of a modifier would be categorized as interacting, as opposed to a non-interacting additive which would coordinate with the oxide support but would do not directly affect the catalytic properties of the surface metal species.[18]

A uniform and high degree of site dispersion of metal oxides enables higher selectivity to propylene, while aggregates such as 3D clusters tend to favor deep oxidation into CO_x.[15,16] While the impregnation method[19] is most often employed to synthesize catalysts for propane ODH, the surface organometallic chemistry (SOMC) grafting technique,[20,21] which is based on anchoring the organometal sites onto the hydroxyl groups, leads to more defined and higher dispersed metal oxide species.[22]

Combinatorial screening, enabled by programmable robotic platforms, offers an opportunity to explore a broad and diverse chemical design space in a high-throughput fashion with exceptional reproducibility and minimal materials investment. Such platforms are ideally suited for depositing organometallic precursors onto solid supports.[23] This allows the syntheses and screening of a large number of catalysts much more rapidly than the conventional approach, thereby reducing the time and cost for material development. An efficient combinatorial screening has been carried out on vanadium-free catalysts for the ODH of ethane and also for the ODH of propane.[24,25] So far, there has not been a wide systematic screening of Mn-based catalysts for the oxidative dehydrogenation of propane. Thus, our approach is to identify synergistic interactions, through high-throughput screening, between additives and Mn which may result in enhanced and stable catalytic performance. Specifically, we performed the high-throughput synthesis of over 150 catalysts by depositing manganese species on a range of supports (TiO_2, ZrO_2, Al_2O_3 and SiO_2) pre-modified with either Lewis acid (Al, Ti, Zn and Zr) or redox-active (Cu, Cr, Ga Ni, V) additives.[4,5,7,12,17,25–31] These additive-types were chosen because Lewis acid sites have been shown to promote propane activation on the catalyst surface,[32] and redox-active sites promote conversion to propylene due to increased hydrogen abstraction.[33] High-throughput activity and durability screening of these bimetallic catalysts for the ODH of propane was then carried out to identify any combination leading to improved reactivity and stability over the non-promoted manganese catalysts.

EXPERIMENTAL SECTION

Materials. Commercially available mesoporous (Selecto) silica support (30–200 μm size, pore size *ca.* 6 nm, surface area 520 m^2/g) was used. γ-Alumina, zirconia, and titania were purchased from Alfa Aesar. All supports were vacuum dried at 200 °C overnight. The amount of organometallic precursor was calculated based on the desired coverage (25, 50, and 75 % of a monolayer). The monolayer was calculated based on the surface area and the OH sites density, which were determined by the Brunauer-Emmett-Teller (BET) and thermogravimetric analyses (TGA), respectively (Table S1). Anhydrous toluene (Aldrich) was purged with N_2, and further dried over activated alumina for 24 h, and tested for dryness with sodium benzophenone ketyl before use. Organometallic precursors for Cu, Ga, Ni, Ti, Zn, and Zr were purchased: trimethylaluminum(III) (>97%, Sigma-Aldrich), bis(dimethylamino-2-propoxy)copper(II) (>97% STREM Chemicals), bis(μ)-dimethylamino)tetrakis(dimethylamino)digallium (98% STREM Chemicals), bis(N,N'-di-t-butylacetamidinato)nickel(II) (99.999% STREM Chemicals), titanium(IV) isopropoxide (99.999% STREM Chemicals), diethylzinc(II) (Sigma-Aldrich), zirconium(IV) tert-

butoxide (99.999% Sigma-Aldrich) and bis(N,N'-di-i-propylpentylamidinato)manganese(II) (98%, STREM Chemicals). The [V(Mes)$_3$(THF)] complex was prepared as reported in the literature.[34] Synthesis of Cr(THF)$_3$(Ph)$_3$ precursor is described in literature.[35]

High-Throughput Catalysis Synthesis. An automated synthesis platform (CM3 Core Module deck, Unchained Labs Inc.) housed in a custom-built N_2-filled glovebox (MB 200B, MBraun), was used for the catalyst syntheses. The CM3 performed both solid and liquid dispensing as well as on-deck stirring. A two-step surface organometallic chemistry (SOMC) process was used for depositing the additives and Mn onto each of the supports as shown in Scheme 1.

Deposition of the additives onto the supports by SOMC. For each support, 25, 50 and 75% coverage of a monolayer by an additive was chosen. Al precursor was not dispensed onto Al_2O_3, Ti precursor was not dispensed onto TiO_2 and Zr precursor was not dispensed onto ZrO_2. For each combination, 200 mg support was weighed in an 8 mL glass vial, preloaded with a magnetic stir bar. Under stirring, the solid supports were then pre-wetted with dry toluene to ensure homogeneous deposition of organometallic precursors. Various stock solutions of organometallic precursors (Al, Cu, Cr, Ga, Ni, Ti, V, Zn, Zr) in toluene were then dispensed into each vial. After dispensing the stock solution, additional toluene was dispensed to adjust the total liquid volume to 4 mL. The 24 well plates of vials were then placed manually onto a shaker plate and let shake for 24 h at 600 rpm. The well plates were then centrifuged (Speedvac Concentrator, Savant SPD121P, ThermoElectron), two well plates at a time, for 10 min and then the supernatant was removed, and 2 mL fresh toluene was added. The procedure was repeated 5 times. After removal of the last supernatant, the vials were then removed from the glovebox and placed onto another shaker (Digital Pulse Mixer, Glas-Col) in a fume hood without the cap to let them dry under air environment over the week-end. This was done to ensure new OH groups would be formed for the deposition of the Mn precursors.

Deposition of the manganese onto the supports by SOMC. For each promoted support, a loading between 0.05 and 2.50 Mn atoms per nm^2 was targeted. 0.05 atoms Mn/nm^2 correspond to 0.57, 2.5, 1.1 and 1.4 surface coverage (%) for Al_2O_3, SiO_2, TiO_2 and ZrO_2, respectively. The dried solids were then brought back into the glovebox for the addition of manganese precursor (bis(N,N'-di-i-propylpentylamidinato)manganese(II)). The same procedure was repeated as above. Each sample was stored outside of the glovebox and tested as-is.

Deposition of manganese on SiO_2 by IW. Mn sites were installed via incipient wetness technique onto SiO_2 support according to literature methods.[36] A nominal loading of 0.05 Mn atoms per nm^2 was achieved by adding SiO_2 with stirring into an aqueous solution prepared by dissolving $Mn(NO_3)_2$ aqueous solution. The mixture was stirred for at least 8 h, and the solids collected via filtration after washing three times. The modified SiO_2 was dried at 120 °C for 6 h, followed by calcination in air at 850 °C for 6 h. Per literature, the Mn species on the support are expected to be Mn_3O_4 ($Mn^{\delta+}$ where $2<\delta<3$).

High-Throughput Catalysis Screening. A 16-channel high-throughput fixed bed system (Flowrence® from Avantium) was used for the catalytic experiments. 50 mg catalyst as-is was mixed with 100 mg Silica Davisil (Sigma-Aldrich) and loaded into a quartz reactor (2 mm ID, 30 mm length). Blank and supports were also tested for comparison and had negligible effects. The reproducibility of the SOMC synthesis and testing were also confirmed by comparing catalytic results of two separate synthetic batches of catalyst, which is shown in Figure S19. The error on the catalytic measurement is less than 2%. Total flowrates for each reactor of 12.7 mL/min were used of which 9.49 mL/min 5% propane/Ar, 2.24 mL/min dry air, and 1 mL/min He. This gives a C_3H_8:O_2 = 1: 1. An O_2 : C_3H_8 ratio of 1 : 1 was used as it was reported to give the best propylene yield.[8] The space velocity was 63,000 h^{-1}. All gases were purchased from Airgas and were UHP grade. The temperatures tested were 300 to 500 °C (5°C/min) with an increment of 50 °C, followed by a stability testing at 500 °C for 25 h. At each temperature, a gas sample was taken automatically, sequentially from reactor #1 to reactor #16, for gas chromatography. Each gas sample was flushed for 11 min before the analysis. Helium was used as internal standard for the gas chromatograph (7890B, Agilent Technologies). The effluent of each reactor was analyzed sequentially by a gas chromatograph, equipped with a thermal conductivity detector (TCD) and two flame ionization detectors (FID) and 4 columns: HP-AL/S (25m x 0.320mm) and DB-FFAP (30m x 0.320mm) (Agilent Technologies), molecular sieve 5A 80/100 6' 1/8" and Hayesep Q 80/100 6' 1/8" (Restek). The main products, besides propylene, were carbon monoxide, carbon dioxide, methane, ethane and ethylene. Carbon balance was between 95 and 100%. The conversion of C_3H_8 was calculated on the basis of the concentration of C_3H_8 in the inlet and outlet of gas flow using He as internal standard using the following equation:

$$C_3H_8\ \text{Conversion}\ (\%) = \frac{([C3H8\ in]-[C3H8\ out])*100}{[C3H8\ in]}$$

The selectivity of each carbon-containing product was calculated by the following equations, as examples:

$$C_3H_6\ \text{Selectivity}\ (\%) = \frac{[C3H6\ out]*100}{[C3H6\ out]+([CH4\ out]+[CO\ out]+[CO2\ out])*(1/3)+([C2H6\ out]+[C2H4\ out])*(2/3)}$$

$$CO\ \text{Selectivity}\ (\%) = \frac{[CO\ out]*100}{[C3H6\ out]+([CH4\ out]+[CO\ out]+[CO2\ out])*(1/3)+([C2H6\ out]+[C2H4\ out])*(2/3)}$$

$$CO_2\ \text{Selectivity}\ (\%) = \frac{[CO2\ out]*100}{[C3H6\ out]+([CH4\ out]+[CO\ out]+[CO2\ out])*(1/3)+([C2H6\ out]+[C2H4\ out])*(2/3)}$$

Characterization. Transmission electron microscopy (TEM) was used to probe for the presence of single atom, nanoparticles or clusters; however, it should be noted that sample preparation for TEM analyses (sonication in ethanol) as well as imaging conditions (a 200 kV electron beam) could change material composition *in situ* (e.g., metal agglomeration). Samples were prepared by dispersing solids

in ethanol via sonication for 30 s. Colloidal suspensions were drop cast onto holey carbon TEM grids. A JEOL JEM-2100F TEM was used for all bright field imaging at 200 kV. A FEI Talos F200x scanning transmission electron microscope (STEM) operated at 200kV was also used for acquiring energy-dispersive X-ray spectra (EDS) and elemental mapping. An aberration-corrected STEM, Thermo Fisher Spectra 200, was also used to obtain atomic-resolution high angle annular dark-field (HAADF) images. Particle size and shape were measured using ImageJ[37] and Gatan Digital Micrograph software. Electron energy loss spectroscopy (EELS) and cathodoluminescence (CL) spectroscopies were acquired using a Spectra 300 STEM with an Attolight CL system. These microscopes were used in coordination with the Center for Nanoscale Materials (CNM) at Argonne National Laboratory. The specific surface area of the catalyst was measured by the BET method at liquid nitrogen temperature using a Micromeritics ASAP2020 surface area analyzer. The samples were first evacuated under dynamic vacuum (< 10-3 torr) at 130 °C overnight to remove the guest molecules and adsorbed moisture before re-measuring the accurate sample weight. Elemental analysis was performed using a Thermo iCap7600 ICP-OES instrument. Approximately 30 mg of sample was digested in 1 mL of HF and subsequently diluted to 11 mL with a 0.9 wt.% HNO_3 aqueous solution. Standards of known concentration were prepared to quantify the samples' metal content. UV–Vis spectroscopic data were obtained on a Shimadzu UV-3600Plus UV–Vis–NIR spectrophotometer. Powder X-ray diffraction (PXRD) patterns were taken on a Rigaku SmartLab Powder X-ray Diffractometer with parallel beam mode and Co radiation with Kβ filter operating at 40 kV and 40 mA. The scan range was between 10° and 60° with 0.005° steps at a collection speed of 1 s/step. X-ray photoelectron spectroscopy (XPS) was performed on at the Surface Analysis Facility at the University of Delaware using a K-Alpha+ XPS system (Thermo Scientific) using an Al K-Alpha X-ray source (hv=1486.6 eV), with a takeoff angle of 35.3° with respect to the analyzer. The high-resolution spectra were collected with a pass energy of 60 eV, and the survey spectra were collected over the 0-1000 eV binding energy range. CasaXPS software was used to analyze and calibrate the raw data. The XPS scale was calibrated to the carbon 1s C-C peak at 284.6 eV.[38,39] Raman spectroscopy was performed using a LabRAM HR Evolution, Horiba with a 532 nm laser.

Results and Discussion

Synthesis on Mn/M_xO_y. Manganese was deposited using bis(N,N'-di-i-propylpentylamidinato)manganese(II) onto the various supports via SOMC at room temperature for 24 h, see Scheme 1. Four loadings of manganese (0.05, 0.25, 1.25 and 2.50 Mn atoms/nm^2) on four supports (Al_2O_3, SiO_2, TiO_2, and ZrO_2) were synthesized. The MnO_x surface density is defined as the number of manganese atoms per square nanometer of the catalyst and provides a convenient parameter for comparing catalysts with a wide range of surface areas.[10] The experimentally determined weight percentages of manganese on all supports are shown in Table 1.

Mn/SiO_2 was also synthesized by incipient wetness technique (IW).[40,41] SiO_2 was chosen because of the high surface area (Table S1) leading to the possibility of high dispersion. Transmission electron microscopy (TEM) images, shown in Fig. S1, taken on Mn/SiO_2 synthesized by the two techniques, revealed micron-sized phase-segregated agglomerates in the case of the IW sample (Fig. S1a). For the SOMC

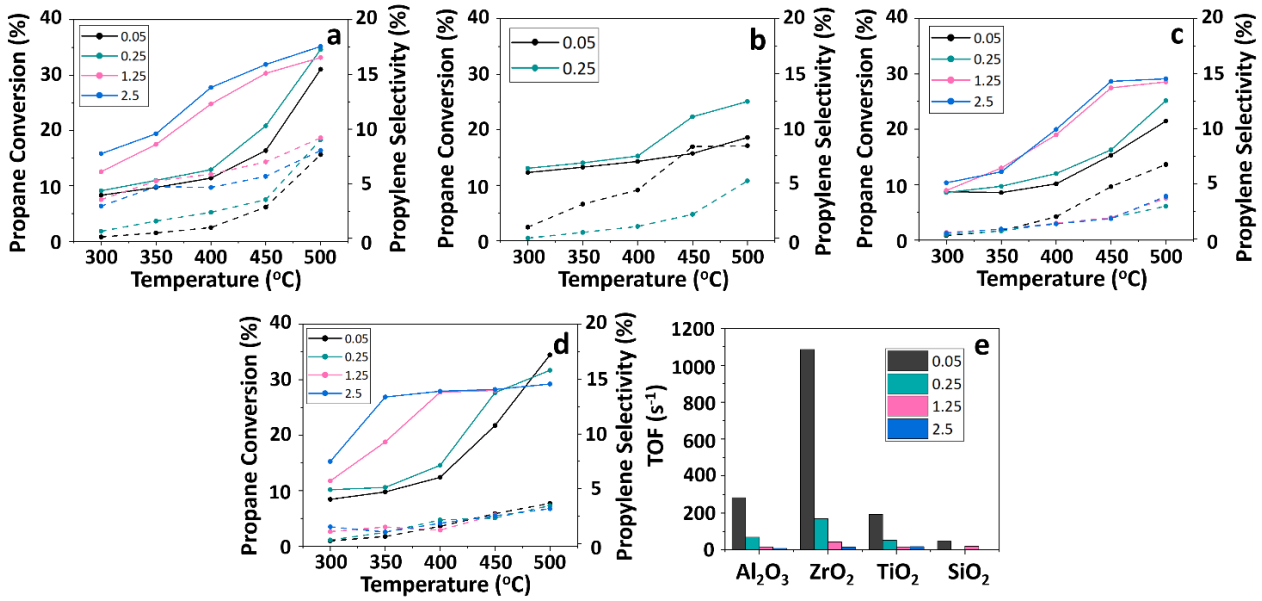

Figure 1. Propane conversion (solid lines) and propylene selectivity (dotted lines) for Mn at loadings of 0.05 Mn atoms/nm^2 (black), 0.25 Mn atoms/nm^2 (teal), 1.25 Mn atoms/nm^2 (pink), and 2.5 Mn atoms/nm^2 (blue) on Al_2O_3 a), SiO_2 b), TiO_2, and ZrO_2 d) as a function of increasing temperature, and TOF at 500 °C for Mn/Al_2O_3, Mn/ZrO_2, Mn/TiO_2 and Mn/SiO_2 at increasing Mn loadings with 0.05 Mn/SiO_2 prepared by SOMC (black) and IW for comparison (pink) e). Reaction conditions were O_2 : C_3H_8 = 1 : 1; GHSV = 63,000 h^{-1}.

Table 1. Actual loadings of additives and manganese on Al_2O_3, ZrO_2, TiO_2, and SiO_2 supports determined by ICP, and the calculated Mn surface density.

Catalyst	Additive wt%	Manganese wt%	Manganese atoms/nm^2
0.05 Mn/Al_2O_3	-	0.007	0.0045
0.25 Mn/Al_2O_3	-	0.038	0.0245
1.25 Mn/Al_2O_3	-	0.191	0.1232
2.5 Mn/Al_2O_3	-	0.283	0.1825
0.05 Mn/V(25)/Al_2O_3	1.7	0.060	0.0387
0.05 Mn/V(50)/Al_2O_3	2.1	0.060	0.0387
0.05 Mn/ZrO_2	-	0.001	0.0044
0.25 Mn/ZrO_2	-	0.006	0.0263
1.25 Mn/ZrO_2	-	0.028	0.1228
2.5 Mn/ZrO_2	-	0.056	0.2456
0.05 Mn/Ni(50)/ZrO_2	0.044	0.001	0.0044
0.05 Mn/Ni(75)/ZrO_2	0.075	0.003	0.0136
0.05 Mn/TiO_2	-	0.004	0.0063
0.25 Mn/TiO_2	-	0.017	0.0266
1.25 Mn/TiO_2	-	0.058	0.0909
2.5 Mn/TiO_2	-	0.059	0.0924
0.05 Mn/SiO_2 (IW)	-	0.118	0.0249
0.05 Mn/SiO_2	-	0.019	0.0040

sample (Fig S1b) there was no agglomerate detected in the TEM images indicating that the grafting technique is preferred for preparing highly dispersed metal oxides onto supports.[15,16]

Catalytic Oxidative Dehydrogenation of Propane. The catalytic activities of the manganese samples were first evaluated as a baseline and to differentiate a synergistic effect between manganese and the second metal from an additive effect.[8] The conversion of propane and propylene selectivity between 300 and 500 °C are shown in Fig 1a-d. Generally, conversion and selectivity increased with increasing temperatures for all supports and loadings of Mn, with 500 °C yielding the highest propane conversion and propylene selectivity. Mn/Al_2O_3 (Fig. 1a) had the highest combination of conversion (31%) and selectivity to propylene (7.6%). Mn/SiO_2 (Fig. 1b) had the lowest propane conversion (18.6%), though the highest propylene selectivity (9.6%). Mn/TiO_2 (Fig. 1c) and Mn/ZrO_2 (Fig. 1d) had propane conversion percentages similar to Mn/Al_2O_3, though the propylene selectivity remained below 10% for both Mn/TiO_2 and Mn/ZrO_2.

Higher Mn loadings resulted in higher propane conversion; however, the propylene selectivity was the highest at the lowest loadings for Mn/SiO_2, Mn/TiO_2, and Mn/ZrO_2, 0.05 atoms/nm^2 (Fig. 1b-d). Catalysts with lower loadings of Mn lead to lower propylene selectivity for Mn/Al_2O_3 (Fig. 1a). However, the TOF increases as the loading of Mn decreases for all supports, shown in Fig. 1e, in agreement with literature on the beneficial effect of highly dispersed metal species onto supports.[42]

In terms of propylene yields, Mn supported on SiO_2, TiO_2, and ZrO_2 show yields less than 2%, while for Mn/Al_2O_3 yields up to 2.5% are observed (Fig. S2). Other products detected in large amounts were CO_2 and CO (Fig. S3). CO_2 selectivities decrease while CO selectivities increase with increasing temperature, due to the propane combustion mechanism switching from oxidizing to reducing conditions.[8] Higher CO_2 selectivity is observed for low concentrations of Mn on supports. This is consistent with literature which claims that exposed support oxide sites favor primary combustion pathways.[15,18]

Following the screening at various temperatures, the catalysts were tested for stability at 500 °C for 20 h (Fig. S4). The propylene yields remain stable for all samples (only 0.05 Mn/supports shown). Despite the stability of Mn/SiO_2, small aggregates were observed after reaction by TEM (Fig. S1c, Fig. S13). Overall, these results suggest that Al_2O_3 offers the best support benefits in terms of high propane conversion and sustained catalytic activity even at prolonged and high temperatures (500 °C) for a monometallic system based on Mn. Based on the above data that allowed for the

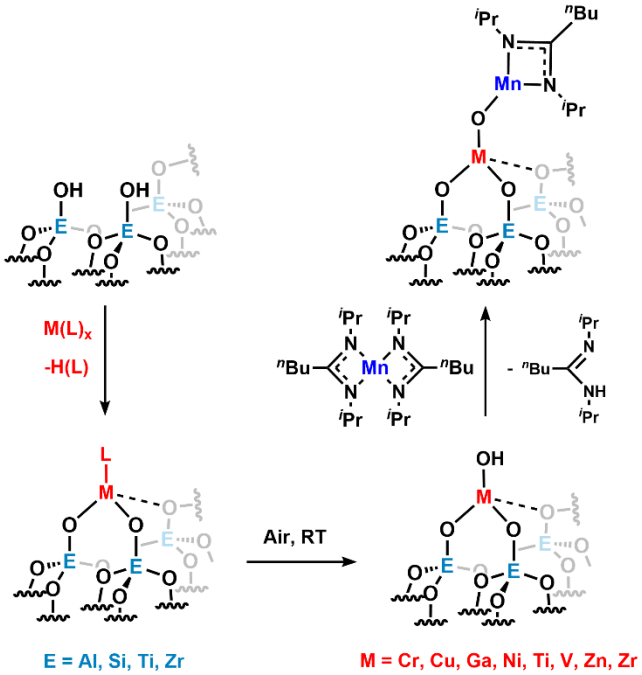

Scheme 1. Multi-step surface organometallic chemistry (SOMC) process for synthesizing bimetallic catalysts: (1) deposition of organometallic additive sites onto an oxide support followed by (2) oxidation in air, then (3) deposition of organomanganese.

identification of systems with highest activity, the lowest target loading of Mn, 0.05 atoms per nm^2, was selected.

Effect of Additives. To understand the effect of additives, the supports were pre-modified with nine different metals, either Lewis acid additives (M = Al, Ti, Zn, Zr) or redox-active additives (M=Cu, Cr, Ga, Ni, V) by SOMC prior to the introduction of the manganese catalytic sites. The amount of additive was determined so that the coverages of manganese oxide and the chosen additive did not exceed monolayer coverages. For Mn/M/support, both 25, 50 and in some cases 75% additive coverages (i.e., percentage with respect to full monolayer coverage, which is estimated based on the surface densities of hydroxyl species) were used, while for M/support only 25 % additive coverage was used. Note that coverage of 25, 50 and 75% corresponds to 1.25, 2.50 and 5 atoms/nm^2, respectively. The weight percentages of each additive were determined experimentally by ICP, shown in Table 1. For each Mn/M/support and M/support, the propylene yield is shown at 300 and 400 °C in Fig. S5 and S6, respectively, and at 500 °C in Fig. 2., and the propane conversion at 500 °C is shown in Fig. S7.

Based on the propylene yields shown in Fig. 2, there were two catalysts with significant improvements in propylene yield compared to supported Mn alone and their additive alone. Those were Mn/V(50)/Al_2O_3 at 12.9% propylene yield and Mn/Ni(50)/ZrO_2 at 13.1% propylene yield. These combinations were characterized further to understand the structural factors that contributed to the improved propylene formation.

Characterization of Mn/V(50)/Al_2O_3. As the tested samples were diluted with silica, samples calcined at 500 °C were used as model for the spent catalysts for characterization. Fig. 3 shows the aberration-corrected HAADF images for Mn/V/Al_2O_3 (Fig. 3a) calcined at 500 °C. In this atomic resolution HAADF image with Z-contrast, several bright dots (circled in Fig. 3a) corresponding to single ion Mn sites can be distinguished on the crystalline metal oxide supports. EDS and EELS were used to identify Mn and V single ions; the EDS mapping results are shown in Fig. 3b-e and the EDS and EELS spectra are shown in Fig. S9. For Mn/V/Al_2O_3 sample, both Mn Kα and V Kα peaks were detected (Fig. S9a). EELS spectra (Fig. S9b) showed the V $L_{2,3}$ election energy loss peak, but the Mn $L_{2,3}$ could not be detected due to the ultra-low loading of Mn. As shown in the EDS mapping of Mn (Fig. 3e), no Mn rich nanoparticles are observed, and all Mn are homogeneously distributed in metal oxide particles.

To better understand the manganese species, 0.05 Mn/V/Al_2O_3 was characterized with Raman spectroscopy, XPS, UV-vis, and XRD. Raman spectroscopy is a valuable tool for determining the oxidation state of manganese oxides, as each Mn oxidation state has a unique signature.[43,44] Raman spectra can indicate long-range crystal structure, but it is also sensitive to local atomic coordination of the oxidized Mn, which makes the technique useful for interrogating low loadings.[43] Care was taken to minimize the laser power and exposure on the sample, as MnO_x is susceptible to laser-induced degradation.[44] Because of that effect and the low concentration of Mn, characterization by Raman must be carefully examined alongside other analytical methods. The formation of more compact crystal structures, such as Mn_2O_3, Mn_3O_4, and MnO, have been identified as potential markers of degradation, and they are also the species of interest in the present study.[44] However, the Raman peak assignments as described are both consistent across different samples and consistent with the results observed for several other analytical techniques described below, and therefore we are confident that the findings presented are accurate. Raman of Mn on Al_2O_3 (Fig. 4a) shows Mn (II-IV) peaks. Mn(II) was the initial oxidation state of the grafted metal from the organomanganese precursor (bis(N,N'-di-i-propylpentylamidinato)manganese(II)).

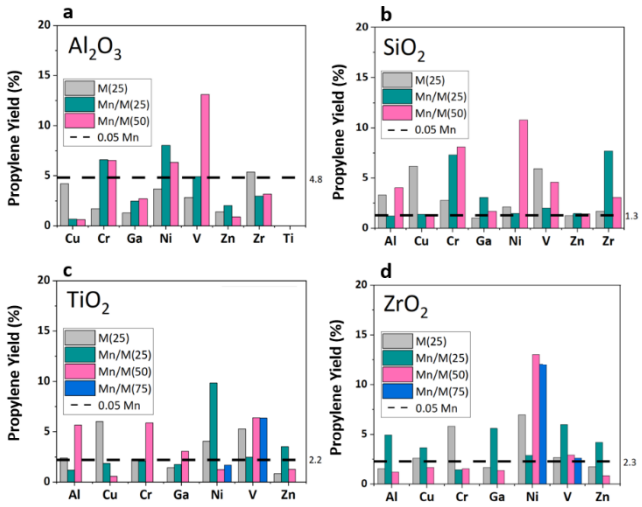

Figure 2. Propylene yield of M/support and Mn/M/support at 500 °C (M = Cu, Cr, Ga, Ni, Ti, V, Zn, and Zr), with Al_2O_3 (a), SiO_2 (b), TiO_2 (c) and ZrO_2 (d), Mn loading is 0.05 atoms/nm^2 and M loadings are 1.25, 2.5 and 5 atoms/nm^2 (25, 50 and 75% coverage, respectively). Propylene yield of 0.05 Mn/support is denoted with a black dotted line.

Once deposited onto Al_2O_3 at the lowest Mn loading, Mn(III) and Mn(IV) were also formed alongside Mn(II) (Fig. 4a). The more oxidized Mn species were likely formed due to interactions with Al vacancies and defects in the support. At Mn loadings of 1.25 atoms/nm^2 and higher, (Fig. 4a) the oxidized Mn (III-IV) predominates and the Mn(II) disappears. This was likely due to increased surface defects as more Mn interacts with Al_2O_3. An early study by Kijlstra et al. showed that the $[Mn(H_2O)_6]^{2+}$ complex grafted onto Al_2O_3 yielded 1:1:1 ratios of Mn(II), Mn(III), and Mn(IV) at low loadings, and predominantly Mn(III) at higher loadings.[45] Raman investigation of Mn/SiO_2 and Mn/TiO_2 yielded similar results, shown in Fig. S11.

Mn was observed via Raman spectroscopy as Mn(II), Mn(III), and Mn(IV) when loaded onto bare alumina,[43] but Mn was not detectable by Raman when grafted onto V/Al_2O_3 (Fig. 4a), which suggests that vanadium promoted highly dispersed Mn sites. These submonolayer Mn ions must be characterized by a surface-sensitive technique, therefore X-

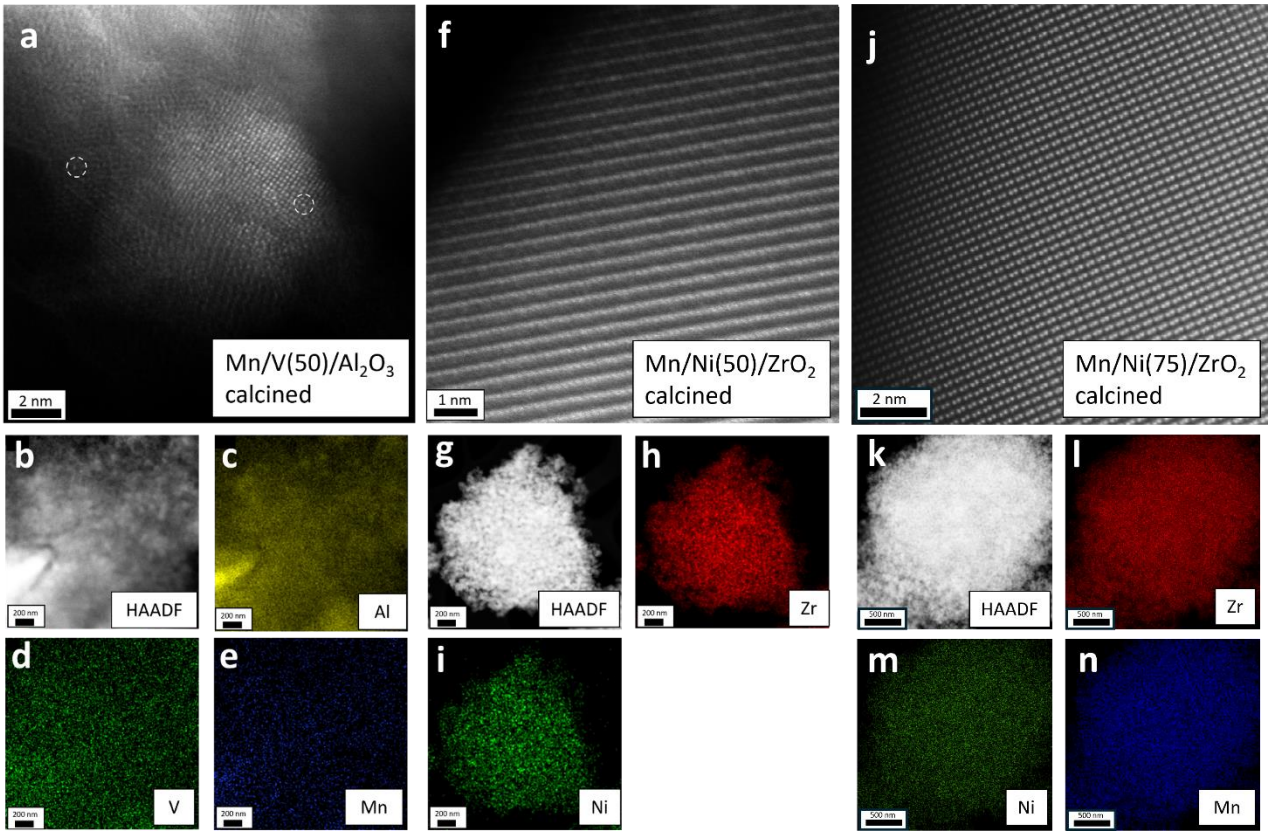

Figure 3. Aberration-corrected atomic-resolution HAADF image for $Mn/V(50)/Al_2O_3$ calcined at 500 °C a) and lower magnification EDS mapping showing the HAADF image b), Al Kα map c), V Kα map d), Mn Kα map e); atomic-resolution HAADF image for $Mn/Ni(50)/ZrO_2$ calcined at 500 °C f), and lower magnification EDS mapping showing the HAADF image g), Zr Lα map h), Ni Kα map i); atomic-resolution HAADF image for $Mn/Ni(75)/ZrO_2$ calcined at 500 °C j) and lower magnification EDS mapping showing the HAADF image k), Zr Lα map l), Ni Kα map m), and Mn Kα map n). The single atom sites observed on $Mn/V(50)/Al_2O_3$ a) are circled in white.

ray photoelectron spectroscopy (XPS) experiments were performed to determine the oxidation state of highly dispersed Mn. It must be noted that direct comparisons of XPS signal intensities between samples can be misleading, as the technique is only semi-quantitative for powder samples without careful calibration and surface-modelling.[46] The Mn 2p and V 2p XPS binding energy regions are shown in Fig. 5a and b, respectively. For all the XPS studies, the sample was examined after calcination in air at 500 °C for 2 h to more closely mimic the surface at reaction temperatures. For Mn/Al_2O_3, and $Mn/V/Al_2O_3$, two Mn $2p_{3/2}$ peaks were observed at 641.4 eV and 643.4 eV with a satellite peak at 647.4 eV, and the corresponding spin-orbit splitting was observed, with Mn $2p_{1/2}$ peaks at 652.6 eV and 654.6 eV, with the satellite peak at 658.6 eV, respectively. The Mn $2p_{3/2}$ peak at 641.4 eV was assigned to Mn(II) in MnO; this assignment was made because the satellite peak at ~6 eV higher than Mn $2p_{3/2}$ is characteristic of MnO and is not present when higher oxidation states of Mn predominate.[47,48] The Mn $2p_{3/2}$ peak at 643.4 eV was assigned to more oxidized Mn, likely Mn(IV) in MnO_2.[49] The XPS results correspond well with the Mn (II-IV) oxidation states observed with Raman spectroscopy on low loading of monometallic Mn on Al_2O_3 (Fig. 5a). Mn 3s has also been used to analyze the Mn oxidation state, however the Mn loading for these samples was too low to observe the already weak 3s peaks.[50,51]

Fig. 5b shows the V 2p binding energy region for V/Al_2O_3 and $Mn/V/Al_2O_3$ after calcination. For each sample, the vanadium signature was deconvoluted into two V $2p_{3/2}$ peaks, and the binding energy for each peak was constrained to the same value for V/Al_2O_3 and $Mn/V/Al_2O_3$. The corresponding V $2p_{1/2}$ peak was also observed but was masked by the high intensity O 1s peak at 531.7 eV and could not be deconvoluted. The two $2p_{3/2}$ peaks were assigned to V(IV) in VO_2 (516.1 eV) and V(V) in V_2O_5 (517.5 eV).[52,53] When Mn and V are both present on the surface, the peak area ratio of V(V) to V(IV) shifted noticeably to 4.0 compared to the baseline 1.3 for V/Al_2O_3. This indicates that during ODH reaction conditions at 500 °C, the $Mn/V/Al_2O_3$ surface consisted of a small amount V(IV) oxides and mainly V_2O_5 species with synergistic interactions with Mn, which supports that vanadium was well-dispersed on Al_2O_3.

The XRD pattern for doped and un-doped Al_2O_3 are shown in Fig. S15. The crystallographic data is not very informative for the Al_2O_3 samples because they were not

highly crystalline, however peaks characteristic of γ-Al_2O_3 can be observed in all samples. There may have been some amount of V(V) insertion into Al_2O_3 based on the similarly sized ionic radii, but the lack of support crystallinity makes this determination not feasible.[54]

In lieu of crystallographic data, the structure of vanadium was interrogated by UV-vis spectroscopy, shown in Fig. 6. The UV spectroscopy shows that for the Mn/V/Al_2O_3 sample, the spectrum is characterized by a strong absorption band centered at 300 nm. This peak has been described by Solsona et al. as a combination of two species with absorption peaks at 250 and 320 nm.[55] These species were assigned to isolated tetrahedral V(V) at the lower wavelength and polymeric V_2O_5 at the higher wavelength, which is also confirmed by XPS (Fig. 5b). The width of the UV band shifts towards higher wavelengths as the loading of vanadium increased, which is indicative of an increase in bulk crystallite V_2O_5.[56] When comparing Mn/V and V alone, the width of the absorption band decreased and blue-shifted on Mn/V, likely due to some electronic interaction between Mn and V species. This observed electronic interaction agrees with Raman and XPS results for Mn as well, as Mn(II) was detected on Mn/V/Al_2O_3 by XPS (Fig. 5a) but could not be detected by Raman, likely due to the increased Mn dispersion when interacting with V. Additionally, there was a higher proportion of V(V) than V(IV) for Mn/V/Al_2O_3 compared to V/Al_2O_3 without Mn (Fig. 5b). These results could indicate a potential charge transfer from V to Mn to form highly isolated V(V) and well-dispersed Mn(II). A similar observation was made by Rybarczyk et al.[57] who reported higher binding energies for V_2O_5 vanadates coordinated to magnesium and zinc at low loadings, which was attributed to increased ionic character of the vanadate species.

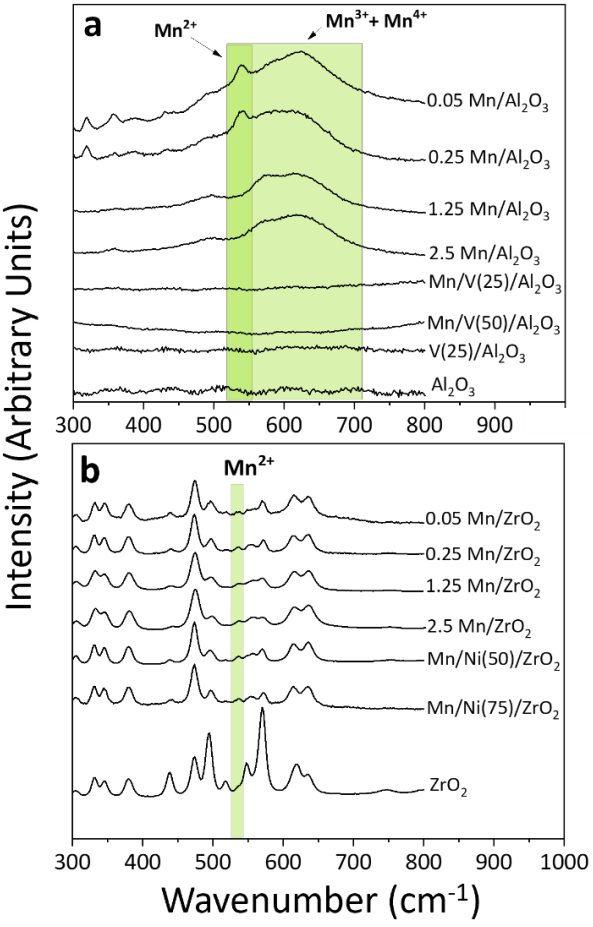

Figure 4. Raman spectra showing the MnO_x region on unpromoted and V-promoted Mn/Al_2O_3 a), and unpromoted and Ni-promoted Mn/ZrO_2 b) at increasing loadings of Mn (0.05, 0.25, 1.25, 2.5 Mn atoms/nm^2). The bare Al_2O_3 and ZrO_2 supports are shown for reference.

The V-induced reduction of Mn would explain the increase in propylene selectivity. Various studies have shown that propylene selectivity is improved by suppression of oxygen availability on the active site. Baldi et al.[8] proposed a mechanism for propane oxidation that emphasized the role of catalyst oxidation state, claiming that low oxidizing ability improved propylene selectivity. More recently, Wang et al.[58] supported this claim and described the mechanism over MnO_x thin films on CeO_2. They explained that oxygen-deficient Mn(II) active sites worked to stabilize propylene on the surface through nucleophilic C=C π-interactions, while simultaneously hindering overoxidation to CO and CO_2 due to the oxygen-deficient environment on MnO sites compared to MnO_2 or Mn_2O_3.[58]

Characterization of Mn/Ni(50)/ZrO_2. Fig. 3f shows the aberration-corrected STEM image for Mn/Ni/ZrO_2 calcined at 500 °C. The EDS maps are shown in Fig. 3g-j, and the EDS and EELS spectra are shown in Fig. S10. For Mn/Ni(50)/ZrO_2, the Ni Kα peak was observed in EDS (Fig. S10a), though no Mn Kα is observed. In EELS spectrum (Fig. S10b) the Ni $L_{2,3}$ peak was likely observed but was barely above the baseline noise. Mn was not observed by EELS for Mn/Ni(50)/ZrO_2 sample. In the atomic resolution HAADF image (Fig. 3f), Zr atomic columns can be observed. Due to lower Z of Mn (Z = 25) or Ni (Z = 28) compared to that of Zr (Z = 40), it is difficult to distinguish Mn and Ni from ZrO_2 crystals using the Z-contrast HAADF imaging approach, and the issue was compounded by the ultra-low loading of Mn. To better visualize the Mn atoms on Ni-added ZrO_2, the Mn/Ni(75)/ZrO_2 sample was also analyzed with HRTEM, shown in Fig. 3j-n, due to its higher loading of Mn atoms (Table 1). On this catalyst, the Mn Kα peak was observed in the EDS spectrum (Fig. S18d), and low magnification EDS mapping of Mn/Ni(75)/ZrO_2 indicates that both Mn and Ni are homogenously distributed in ZrO_2 nanoparticles (Fig. 3k-n). Cathodoluminescence (CL) is sensitive to trace amount of Mn in oxides. Fig. S18a-c shows the CL results, including the CL spectrum of Mn/Ni(75)/ZrO_2 calcined at 500 °C (Fig. S18c). A broad peak at 536.7 nm with FWHM of 115 nm and a sharp peak at 691.9 nm with FWHM of 4 nm are observed. The broad peak at 536.7 nm can be assigned to the 3d[5]

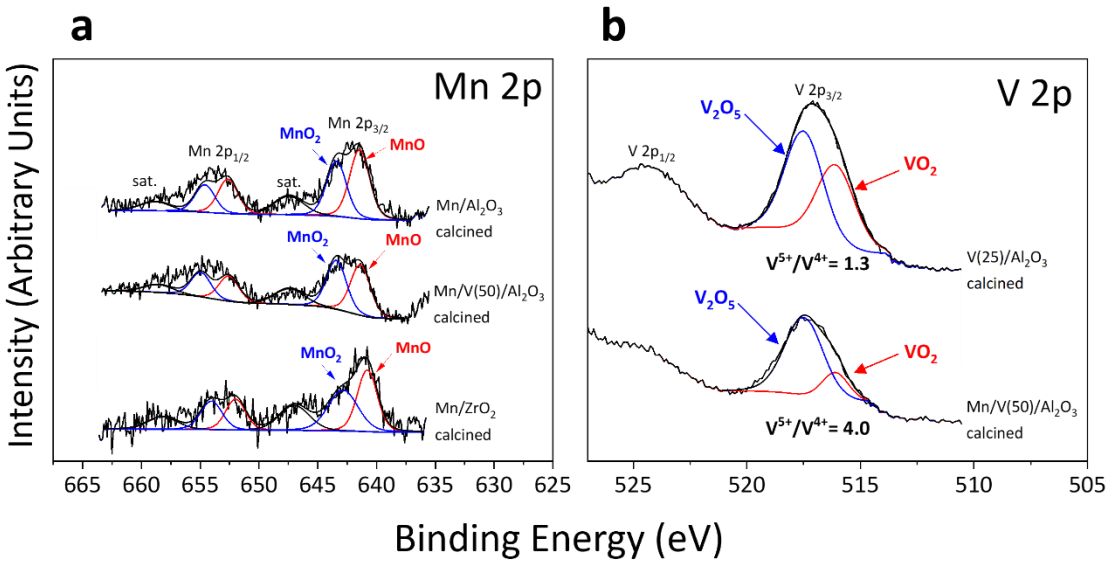

Figure 5. XPS binding energy regions for Mn 2p a) and V 2p b) for 0.05 Mn/Al_2O_3, 0.05 $Mn/V(50)/Al_2O_3$, 0.05 Mn/ZrO_2, and $V(25)/Al_2O_3$ after calcination at 500 °C.

($^4T_{1g}$)–$3d^5$ ($^6A_{1g}$) transition of Mn^{2+} ions in ZrO_2,[59,60] and the sharp peak at 691.9 nm can be assigned to Mn^{4+} ions.[61]

The oxidation state of Mn on ZrO_2 at various loadings and 0.05 $Mn/Ni/ZrO_2$ at increasing Ni loadings was observed by Raman spectroscopy in Fig. 4b, which shows the Mn(II) signal present on all scans except for bare ZrO_2. The Mn(III) and Mn(IV) species may have been present, but they were obscured by ZrO_2 peaks. Similar studies have reported that the dominant oxidation state for low-loading Mn on ZrO_2, was Mn(II).[62–65] The intensity of the Mn(II) peak also appeared to increase for $Mn/Ni/ZrO_2$ catalysts compared to unpromoted 0.05 Mn/ZrO_2. This increase in Mn uptake correlates well with the ICP data in Table 1, which shows a 3-fold increase in Mn wt.% from 0.05 Mn/ZrO_2 (0.001 wt.%) to 0.05 $Mn/Ni(75)/ZrO_2$ (0.003 wt.%).

To further interrogate the chemical structure, XPS experiments were conducted for $Ni(25)/ZrO_2$, Mn/ZrO_2, and $Mn/Ni(50)/ZrO_2$ calcined at 500 °C for 2 h (Fig. 5a and Fig. S16). The Mn 2p binding energy region shown in Fig. 5a for Mn/ZrO_2 revealed Mn species similar to those observed on alumina support. Both MnO and MnO_2 were detected, while the Mn(IV) could not be observed by Raman spectroscopy in Fig. 4b, *vide supra*. The XPS results confirmed that the Mn(II) species was the more prevalent oxidation state. The Mn 2p region was also collected for $Mn/Ni/ZrO_2$, however the Ni LMM Auger peak overlapped with the Mn 2p region, fully overpowering any signal from Mn, and the Mn 3s signal was too weak to provide clarity.[66] In Fig. S16, the Ni 2p region was shown for $Ni(25)/ZrO_2$ and $Mn/Ni(50)/ZrO_2$. The peaks observed on Ni/ZrO_2 and $Mn/Ni/ZrO_2$ were similar, showing that the electronic state of Ni was unchanged by the presence of Mn. The Ni 2p peaks observed were characteristic of mixed nickel oxides.[67–69]

Powder X-ray diffraction (PXRD) experiments were performed on un-modified and modified ZrO_2 samples to investigate changes in the support crystal structure. The full diffraction patterns for ZrO_2 samples were shown in Fig. S17, and all diffraction patterns were characteristic of monoclinic ZrO_2 (JCPPDS 37-1484), with no other species detected. The zoomed-in (111) peak of monoclinic ZrO_2 is shown in Fig. 7, which displays the shift in the diffraction peaks after ZrO_2 was doped with Mn and Ni. This peak shift arises from changing lattice parameters, detailed in Table S4. When Mn was deposited onto ZrO_2 (Mn/ZrO_2), the lattice parameters remained largely unchanged, but the overall lattice strain increased by 241%. When Ni was deposited (Ni/ZrO_2), the lattice parameter a decreased by 3.2%, the lattice parameter b remained relatively unchanged, and the lattice parameter c increased by 3.2%. This change was accompanied by a significant increase in lattice strain: 138% more strain compared to ZrO_2.

When both Mn and Ni had been deposited, the $Mn/Ni/ZrO_2$ as prepared had similar changes in lattice parameters (*a*: -3.0%, c: +3.5%) as well as $Mn/Ni/ZrO_2$ calcined (*a*: -3.0%, b: +3.4%). The lattice strain for $Mn/Ni/ZrO_2$ as prepared increased by 253.8% compared to bare ZrO_2 and unit cell volume increased slightly by 1%. After calcination, the lattice strain for $Mn/Ni/ZrO_2$ had decreased slightly (still 169.2% more than bare ZrO_2) but the unit cell volume remained higher than bare ZrO_2.

Zr(IV) cations in 7-coordinated monoclinic ZrO_2 structure have an ionic radius of 0.78 Å.[63] After the organometallic nickel deposited onto ZrO_2, Ni(II) (0.77-0.83 Å depending on coordination)[70] was introduced onto the ZrO_2 surface. The Ni(II) ion has a similar ionic radius to Zr(IV), therefore the sharp increase in lattice strain for Ni/ZrO_2 indicated incorporation of Ni(II) into the ZrO_2 lattice, substituting Zr(IV) ions.[65] The Mn catalyst without Ni also exhibited substitutional behavior, shown by the significant increase in lattice strain and changes in lattice parameters for Mn/ZrO_2. This was no surprise, as the Mn(II) ion (0.80-0.96 Å, depending on coordination)[63] has been well-studied for substitution into the ZrO_2 lattice.[63–65] When Mn was deposited onto Ni/ZrO_2 however, the lattice became even more highly strained (Table S4) and the unit cell volume increased, indicating higher additive uptake. Substitution of Ni into the ZrO_2 lattice aided in highly dispersed Mn uptake, resulting in better propylene yield (Fig. 2).

Crystalline materials with induced lattice strain have also been shown to improve the solubility of ionic dopants. This lattice strain effect has been studied by Ferrerra et al., who predicted that Ca(II) ions were more soluble in strained $LaNbO_4$.[71] Additionally this phenomenon has been widely studied in semiconductor research, with several studies demonstrating that induced lattice strain on semiconductor materials enhanced dopant solubility.[72–74]

Catalyst Stability Following the screening at various temperatures, the reaction was monitored for an additional 25 h at 500 °C for all the mono- and bi-metallic samples for evaluating their stability (Fig. S8). Fig. 8a compares the individual activities of 0.05 $Mn/V(50)/Al_2O_3$ (12.9 %) in terms of propylene yield as a function of time compared to Mn alone and additive alone. $Mn/V(50)/Al_2O_3$ shows significantly higher activity and stability for the propylene yield at 500 °C in comparison with 0.05 Mn/Al_2O_3 and V/Al_2O_3, as shown in Fig. 8a. Additionally, the poor activity of V/Al_2O_3 cannot be attributed to particle agglomeration, as no nanoparticles were detected on the spent catalyst (Fig. S12) The deactivation rate for $Mn/V(50)/Al_2O_3$, 0.0009 h^{-1}, is lower in

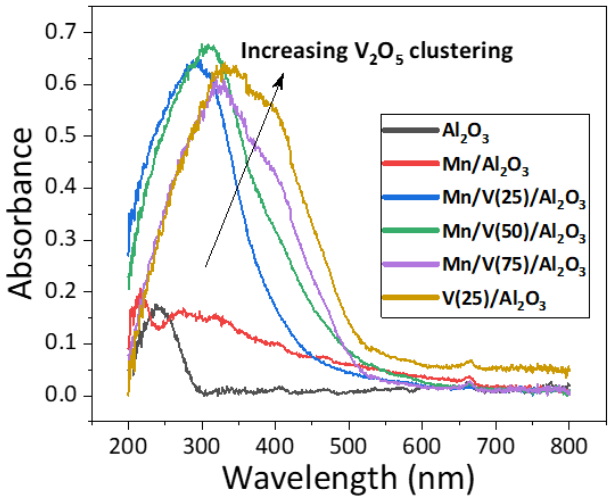

Figure. 6. UV-Vis spectra for Al_2O_3, 0.05 Mn/Al_2O_3, V/Al_2O_3, and 0.05 $Mn/V/Al_2O_3$ at varying V loadings.

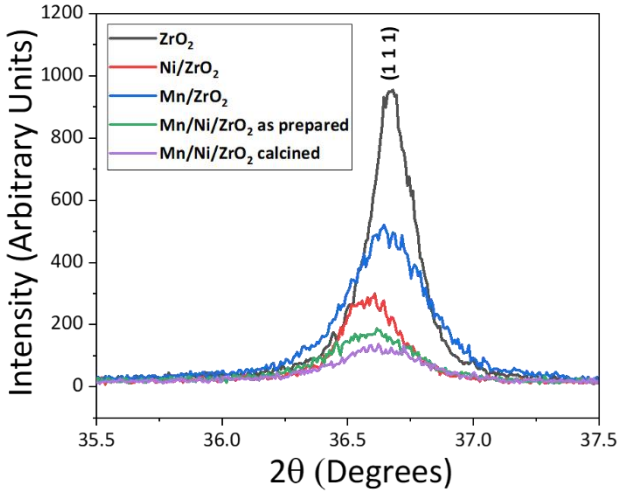

Figure 7. (111) ZrO_2 plane by X-ray diffraction of ZrO_2, $Ni(25)/ZrO_2$, 0.05 Mn/ZrO_2, 0.05 $Mn/Ni(50)/ZrO_2$ as-prepared and 0.05 $Mn/Ni(50)/ZrO_2$ calcined at 500 °C.

comparison to that of V alone, 0.0219 h^{-1} (Table S2) while that for Mn/Al_2O_3 was negative (-0.0108) because of the initial increase in yield.

In addition, the selectivity to CO over CO_2 for $Mn/V/Al_2O_3$ is increased compared to 0.05 Mn/Al_2O_3 (Fig. 8e), likely due to competing reactions such as propane steam reforming (3) and propylene steam reforming (4) considering that two moles of H_2O are formed for every one mole of propylene (1). However, increased selectivity to CO makes the combination Mn/V attractive for processes with low CO_2 emission.

Propane steam reforming

$$C_3H_8 + 3\,H_2O \leftrightarrow 3\,CO + 7\,H_2 \quad (3)$$

Propylene steam reforming

$$C_3H_6 + 3\,H_2O \leftrightarrow 3\,CO + 6\,H_2 \quad (4)$$

Fig. 8b shows the propylene yields over time for Mn/ZrO_2, $Ni(25)/ZrO_2$, $Ni(50)/ZrO_2$, and $Mn/Ni(50)/ZrO_2$ at 500 °C. The same trend is observed as described for $Mn/V/Al_2O_3$. For 0.05 $Mn/Ni/ZrO_2$, the propylene yield increased from 1.3% for Mn/ZrO_2 alone to 13.1% for Mn/Ni catalyst. Additionally, the TOF for Mn/ZrO_2 upon addition of Ni improved from 18 to 107 min^{-1} (Table S2). The yield is stable over the 25-h tested (k_d = -0.001 h^{-1} while that of $Ni(25)/ZrO_2$ decays rapidly k_d = 0.0179 h^{-1}), and this decay cannot be explained by nickel sintering (Fig. S14). Fig. 8d shows the propylene selectivity vs propane conversion. While there is little effect on the propane conversion for the $Mn/Ni/ZrO_2$ compared to the Mn or Ni alone at a similar Mn loading (0.05), the propylene selectivity is enhanced significantly to 85% at 500 °C. The selectivity towards by-products (CO and CO_2) is shown in Fig. 8f, and in particular the selectivities towards both CO_2 and CO are lower for the Mn/Ni compared to the Mn or Ni alone. The higher selectivity to CO observed on monometallic Ni/ZrO_2 and 0.05 Mn/ZrO_2 could be due to the propane or propylene steam reforming reactions (3,4). With the introduction of H_2 from steam reforming, the

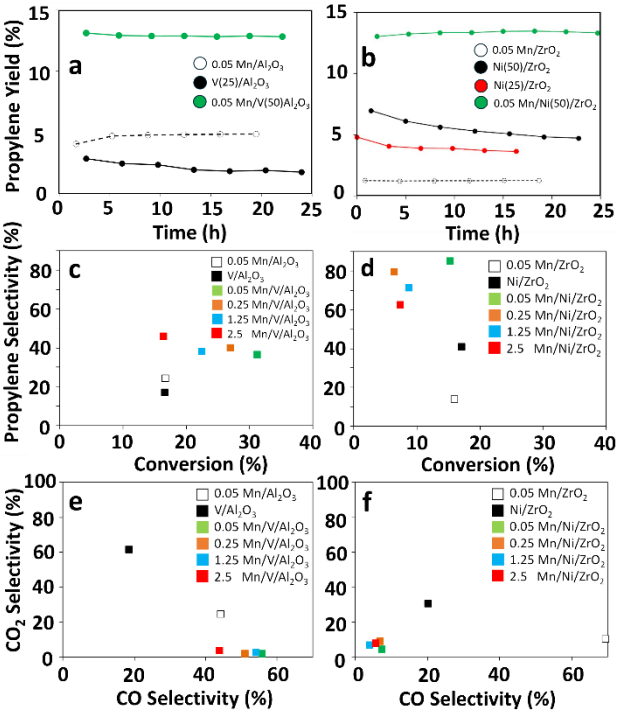

Figure 8. Propylene yields, propane conversion vs. propylene selectivity, CO selectivity vs. CO_2 selectivity for $Mn/V(50)/Al_2O_3$ a, c and e) and $Mn/Ni(50)/ZrO_2$ b, d and f). Manganese loadings: 0.05 (green), 0.25 (orange), 1.25 (blue) and 2.5 (red) atoms/nm^2. Comparison with $V(25)/Al_2O_3$, $Ni(25)/ZrO_2$ (black symbols) and $0.05\ Mn/Al_2O_3$ and $0.05\ Mn/ZrO_2$ (dotted line, open symbols).

reverse water-gas shift (RWGS, 5) could further increase selectivity to CO. The RWGS reaction has been shown to be quite favorable at high temperatures on Ni-based and Mn-based catalysts.[75,76]

Reverse water-gas shift

$$CO_2 + H_2 \leftrightarrow CO + H_2O \qquad (5)$$

The observed propylene yields of up to 13% at reaction conditions such as propane : O_2 = 1 : 1 and 300-500 °C were improved over state-of-the-art yields of 2-10% using supported Mn catalysts at similar temperatures but under non-oxidative dehydrogenation.[8] For non-Mn compositions, Hermans et al. have reported several studies involving boron-based catalysts, including boron nitride (87.4% selectivity to propylene, 5% propane conversion) and acid-treated, activated carbon-supported boron (87% propylene selectivity, 5% propane conversion).[77] For V-based systems, Guo et al. reported a propylene selectivity of 70%, at a propane conversion of 20%, while Alasiri reported a 100% selectivity at 4.8% conversion for a Mo/V catalyst at 500 °C.[78,79] More recently, catalysts and achieved 96% propylene selectivity and 47% propane conversion. In this study, $0.05\ Mn/Ni(50\%)/ZrO_2$ showed high propylene selectivity (85%) at a conversion of nearly 15%.

Conclusion

In summary, we reported the effect of submonolayers of additive ions (M = Al, Cu, Cr, Ga, Ni, Ti, V, Zn, and Zr) with 4 different supports (Al_2O_3, SiO_2, TiO_2, and ZrO_2) on manganese-based active sites for the oxidative dehydrogenation of propane to propylene. Over 150 catalysts were synthesized using an automated robotic platform followed by activity and stability screening with a high-throughput reactor system, and the two best performing catalysts were investigated further using HRTEM, EDS, EELS, XPS, XRD, Raman spectroscopy, and UV-vis spectroscopy. The additives affected the performance of the catalysts; Ni was found to be a very beneficial additive on ZrO_2, and on Al_2O_3, V was found the best. $0.05\ Mn/V/Al_2O_3$ and $0.05\ Mn/Ni/ZrO_2$ catalysts were examined in depth because they showed the highest combined conversion and propylene selectivities (31/41% and 15/85%), with excellent stability at 500 °C for 25 h. The grafting technique used for depositing additives and manganese allowed for atomically dispersed species evidenced by HRTEM after treatment at 500 °C, as well as Mn(II) and Ni(II) substitution into the ZrO_2 lattice which likely increased Mn dispersion. The presence of V increased the dispersion of Mn on Al_2O_3, as well as stabilized the reduced Mn(II) oxidation state, which enhanced propylene selectivity. The remarkably enhanced robustness of these bimetallic catalysts against agglomeration were provided by stabilization of atomically dispersed Mn enhanced by the addition of Ni and V additives.

ASSOCIATED CONTENT

Supporting Information. Surface area and ICP analysis, additional HRTEM images and EDS, extended catalysis results including propylene yields, propane conversions, CO/CO_2 selectivities, and TOF calculations, EELS spectroscopy, additional Raman spectroscopy and XPS results, and XRD fitting parameters. This material is available free of charge via the Internet at http://pubs.acs.org.XXXX.

AUTHOR INFORMATION

Corresponding Authors

Magali Ferrandon - *Chemical Sciences and Engineering Division, Argonne National Laboratory, Lemont, Illinois 60439, United States;* orcid.org/0000-0003-2544-6466
Email: ferrandon@anl.gov

Massimiliano Delferro - *Chemical Sciences and Engineering Division, Argonne National Laboratory, Lemont, Illinois 60439, United States;* orcid.org/0000-0002-4443-165X;
Email: delferro@anl.gov

Authors

Carly Byron - *Chemical Sciences and Engineering Division, Argonne National Laboratory, Lemont, Illinois 60439, United States;* orcid.org/0000-0002-1716-5659; Email: cbyron@anl.gov

Patrica Anne Ignacio-de Leon - *Advanced Materials Division, Argonne National Laboratory, Lemont, Illinois 60439, United States;* Email: patricia.ignaciodeleon@donaldson.com

Jacob Bryant- *Chemical Sciences and Engineering Division, Argonne National Laboratory, Lemont, Illinois 60439, United States;* orcid.org/0000-0002-7737-4604*;* Email: bryantj@anl.gov
Ryan Langeslay - *Chemical Sciences and Engineering Division, Argonne National Laboratory, Argonne, Lemont, Illinois 60439, United States;* Email: somesed@yahoo.com
Louisa Savereide - *Department of Chemical and Biological Engineering, Northwestern University, Evanston, Illinois 60208, United States;* Email: l.savereide@gmail.com
Jianguo Wen - *Center for Nanoscale Materials Argonne National Laboratory, Argonne, Lemont, Illinois 60439, United States;* orcid.org/0000-0002-3755-0044*;* Email: jwen@anl.gov
Jeffrey Camacho-Bunquin - *Department of Chemical and Biological Engineering, Northwestern University, Evanston, Illinois 60208, United States;* orcid.org/0000-0003-2297-3404*;* Email: jeffrey.c.bunquin@exxonmobil.com
Justin M. Notestein - *Department of Chemical and Biological Engineering, Northwestern University, Evanston, Illinois 60208, United States;* orcid.org/0000-0003-1780-7356*;* Email: j-notestein@northwestern.edu

Present Addresses
†If an author's address is different than the one given in the affiliation line, this information may be included here.

Author Contributions
The manuscript was written through contributions of all authors. / All authors have given approval to the final version of the manuscript.

Funding Sources
Any funds used to support the research of the manuscript should be placed here (per journal style).

ACKNOWLEDGMENT

The present work was supported by the U.S. Department of Energy (DOE), Office of Basic Energy Sciences, Division of Chemical Sciences, Geosciences, and Biosciences, Catalysis Science Program under contract No. DE-AC-02-06CH11357. This research used resources of the Advanced Photon Source and the Center for Nanoscale Materials, U.S. Department of Energy (DOE) Office of Science User Facilities operated for the DOE Office of Science by Argonne National Laboratory under Contract No. DE-AC02-06CH11357.

ABBREVIATIONS

REFERENCES

(1) Phung, T. K.; Pham, T. L. M.; Vu, K. B.; Busca, G. (Bio)Propylene Production Processes: A Critical Review. *J. Environ. Chem. Eng.* **2021**, *9*, 105673.

(2) Carter, J. H.; Bere, T.; Pitchers, J. R.; Hewes, D. G.; Vandegehuchte, B. D.; Kiely, C. J.; Taylor, S. H.; Hutchings, G. J. Direct and Oxidative Dehydrogenation of Propane: From Catalyst Design to Industrial Application. *Green Chem.* **2021**, *23*, 9747–9799.

(3) Zuo, C.; Su, Q. Research Progress on Propylene Preparation by Propane Dehydrogenation. *Molecules* **2023**, *28*, 3594.

(4) Sattler, J. J. H. B.; Ruiz-Martinez, J.; Santillan-Jimenez, E.; Weckhuysen, B. M. Catalytic Dehydrogenation of Light Alkanes on Metals and Metal Oxides. *Chem. Rev.* **2014**, *114*, 10613–10653.

(5) Gambo, Y.; Adamu, S.; Abdulrasheed, A. A.; Lucky, R. A.; Ba-Shammakh, M. S.; Hossain, Mohammad. M. Catalyst Design and Tuning for Oxidative Dehydrogenation of Propane – A Review. *Appl. Catal., A* **2021**, *609*, 117914.

(6) Jiang, X.; Sharma, L.; Fung, V.; Park, S. J.; Jones, C. W.; Sumpter, B. G.; Baltrusaitis, J.; Wu, Z. Oxidative Dehydrogenation of Propane to Propylene with Soft Oxidants via Heterogeneous Catalysis. *ACS Catal.* **2021**, *11*, 2182–2234.

(7) Kondratenko, E. V.; Cherian, M.; Baerns, M. Mechanistic Aspects of the Oxidative Dehydrogenation of Propane over an Alumina-Supported $VCrMnWO_x$ Mixed Oxide Catalyst. *Catal. Today* **2005**, *99*, 59–67.

(8) Baldi, M.; Finocchio, E.; Pistarino, C.; Busca, G. Evaluation of the Mechanism of the Oxy-Dehydrogenation of Propane over Manganese Oxide. *Appl. Catal., A* **1998**, *173*, 61–74.

(9) Jibril, B. Y. Effects of Feed Compositions on Oxidative Dehydrogenation of Propane over Mn–P–O Catalyst. *Ind. Eng. Chem. Res.* **2005**, *44*, 702–706.

(10) Neal, L. M.; Yusuf, S.; Sofranko, J. A.; Li, F. Oxidative Dehydrogenation of Ethane: A Chemical Looping Approach. *Energy Technol.* **2016**, *4*, 1200–1208.

(11) Al-Hazmi, M. H.; Odedairo, T.; Al-Dossari, A. S.; Choi, Y. Revisiting Oxidative Dehydrogenation of Ethane by W Doping into MoVMn Mixed Oxides at Low Temperature. *Adv. Phys. Chem.* **2015**, *2015*, 1–9.

(12) Li, X.; Lunkenbein, T.; Pfeifer, V.; Jastak, M.; Nielsen, P. K.; Girgsdies, F.; Knop-Gericke, A.; Rosowski, F.; Schlögl, R.; Trunschke, A. Selective Alkane Oxidation by Manganese Oxide: Site Isolation of MnO_x Chains at the Surface of $MnWO_4$ Nanorods. *Angew. Chem., Int. Ed.* **2016**, *55*, 4092–4096.

(13) Yusuf, S.; Neal, L. M.; Li, F. Effect of Promoters on Manganese-Containing Mixed Metal Oxides for Oxidative Dehydrogenation of Ethane via a Cyclic Redox Scheme. *ACS Catal.* **2017**, *7*, 5163–5173.

(14) Wu, Z.; Jiang, B.; Liu, Y. Effect of Transition Metals Addition on the Catalyst of Manganese/Titania for Low-Temperature Selective Catalytic Reduction of Nitric Oxide with Ammonia. *Appl. Catal., B* **2008**, *79*, 347–355.

(15) Khodakov, A.; Olthof, B.; Bell, A. T.; Iglesia, E. Structure and Catalytic Properties of Supported Vanadium Oxides: Support Effects on Oxidative Dehydrogenation Reactions. *J. Catal.* **1999**, *181*, 205–216.

(16) Dai, G. L.; Li, Z. H.; Lu, J.; Wang, W. N.; Fan, K. N. Deep Oxidations in the Oxidative Dehydrogenation Reaction of Propane over V_2O_5(001): Periodic Density Functional Theory Study. *J. Phys. Chem. C* **2012**, *116*, 807–817.

(17) Yang, S.; Iglesia, E.; Bell, A. T. Oxidative Dehydrogenation of Propane over $V_2O_5/MoO_3/Al_2O_3$ and $V_2O_5/Cr_2O_3/Al_2O_3$: Structural Characterization and Catalytic Function. *J. Phys. Chem. B* **2005**, *109*, 8987–9000.

(18) Cherian, M.; Gupta, R.; Someswara Rao, M.; Deo, G. Effect of Modifiers on the Reactivity of Cr_2O_3/Al_2O_3 and Cr_2O_3/TiO_2 Catalysts for the Oxidative Dehydrogenation of Propane. *Catal. Lett.* **2003**, *86*, 179–189.

(19) Wang, Z.; Qin, Y.; Pan, F.; Li, Z.; Zhang, W.; Wu, F.; Chen, D.; Wen, W.; Li, J. Mesoporous Silica-Supported Manganese Oxides for Complete Oxidation of Volatile Organic Compounds: Influence of Mesostructure, Redox Properties, and Hydrocarbon Dimension. *Ind. Eng. Chem. Res.* **2018**, *57*, 7374–7382.

(20) Marks, T. J. Surface-Bound Metal Hydrocarbyls. Organometallic Connections between Heterogeneous and Homogeneous Catalysis. *Acc. Chem. Res.* **1992**, *25*, 57–65.

(21) Copéret, C.; Comas-Vives, A.; Conley, M. P.; Estes, D. P.; Fedorov, A.; Mougel, V.; Nagae, H.; Núñez-Zarur, F.; Zhizhko, P. A. Surface Organometallic and Coordination Chemistry toward Single-Site Heterogeneous Catalysts: Strategies, Methods, Structures, and Activities. *Chem. Rev.* **2016**, *116*, 323–421.

(22) K. Samantaray, M.; Pump, E.; Bendjeriou-Sedjerari, A.; D'Elia, V.; A. Pelletier, J. D.; Guidotti, M.; Psaro, R.; Basset, J.-M. Surface Organometallic Chemistry in Heterogeneous Catalysis. *Chem. Soc. Rev.* **2018**, *47*, 8403–8437.

(23) Ferrandon, M. S.; Byron, C.; Celik, G.; Zhang, Y.; Ni, C.; Sloppy, J.; McCormick, R. A.; Booksh, K.; Teplyakov, A. V.; Delferro, M. Grafted Nickel-Promoter Catalysts for Dry Reforming of Methane Identified through High-Throughput Experimentation. *Appl. Catal., A* **2022**, *629*, 118379.

(24) Grubert, G.; Kondratenko, E.; Kolf, S.; Baerns, M.; van Geem, P.; Parton, R. Fundamental Insights into the Oxidative Dehydrogenation of Ethane to Ethylene over Catalytic Materials Discovered by an Evolutionary Approach. *Catal. Today* **2003**, *81*, 337–345.

(25) Buyevskaya, O. V.; Brückner, A.; Kondratenko, E. V.; Wolf, D.; Baerns, M. Fundamental and Combinatorial Approaches in the Search for and Optimisation of Catalytic Materials for the Oxidative Dehydrogenation of Propane to Propene. *Catal. Today* **2001**, *67*, 369–378.

(26) Al-Zahrani, S. M.; Jibril, B. Y.; Abasaeed, A. E. Propane Oxidative Dehydrogenation over Alumina-Supported Metal Oxides. *Ind. Eng. Chem. Res.* **2000**, *39*, 4070–4074.

(27) Palacio, L. A.; Echavarría, A.; Sierra, L.; Lombardo, E. A. Cu, Mn and Co Molybdates Derived from Novel Precursors Catalyze the Oxidative Dehydrogenation of Propane. *Catal. Today* **2005**, *107–108*, 338–345.

(28) Boizumault-Moriceau, P.; Pennequin, A.; Grzybowska, B.; Barbaux, Y. Oxidative Dehydrogenation of Propane on Ni□Ce□O Oxide: Effect of the Preparation Method, Effect of Potassium Addition and Physical Characterization. *Appl. Catal., A* **2003**, *245*, 55–67.

(29) Liu, G.; Zeng, L.; Zhao, Z. J.; Tian, H.; Wu, T.; Gong, J. Platinum-Modified ZnO/Al_2O_3 for Propane Dehydrogenation: Minimized Platinum Usage and Improved Catalytic Stability. *ACS Catal.* **2016**, *6*, 2158–2162.

(30) Xie, Q.; Zhang, H.; Kang, J.; Cheng, J.; Zhang, Q.; Wang, Y. Oxidative Dehydrogenation of Propane to Propylene in the Presence of HCl Catalyzed by CeO_2 and NiO-Modified CeO_2 Nanocrystals. *ACS Catal.* **2018**, *8*, 4902–4916.

(31) Jibril, B. Y.; Al-Kinany, M. C.; Al-Khowaiter, S. H.; Al-Drees, S. A.; Al-Megren, H. A.; Al-Dosari, M. A.; Al-Rasheed, R. H.; Al-Zahrani, S. M.; Abasaeed, A. E. Performances of New Kieselguhr-Supported Transition Metal Oxide Catalysts in Propane Oxydehydrogenation. *Catal. Commun.* **2006**, *7*, 79–85.

(32) Kantserova, M. R.; Vlasenko, N. V.; Orlyk, S. M.; Veltruska, K.; Matolinova, I. Effect of Acid–Base Characteristics of In_2O_3-Al_2O_3 (ZrO_2) Compositions on Their Catalytic Properties in the Oxidative Dehydrogenation of Propane to Propylene with CO_2. *Theor. Exp. Chem.* **2019**, *55*, 207–214.

(33) Pantazidis, A.; Auroux, A.; Herrmann, J. M.; Mirodatos, C. Role of Acid—Base, Redox and Structural Properties of VMgO Catalysts in the Oxidative Dehydrogenation of Propane. *Catal.Today* **1996**, *32*, 81–88.

(34) Vivanco, M.; Ruiz, J.; Floriani, C.; Chiesi-Villa, A.; Rizzoli, C. Chemistry of the Vanadium-Carbon σ Bond. 1. Insertion of Carbon Monoxide, Isocyanides, Carbon Dioxide, and Heterocumulenes into the V-C Bond of Tris(Mesityl)Vanadium(III). *Organometallics* **1993**, *12*, 1794–1801.

(35) Herwig, W.; Zeiss, H. H. TRIPHENYLCHROMIUM1. *J. Am. Chem. Soc.* **1957**, *79*, 6561–6561.

(36) Hou, S.; Cao, Y.; Xiong, W.; Liu, H.; Kou, Y. Site Requirements for the Oxidative Coupling of Methane on SiO_2-Supported Mn Catalysts. *Ind. Eng. Chem. Res.* **2006**, *45*, 7077–7083.

(37) Schneider, C. A.; Rasband, W. S.; Eliceiri, K. W. NIH Image to ImageJ: 25 Years of Image Analysis. *Nature Methods* **2012**, *9*, 671-675.

(38) Gammon, W. J.; Kraft, O.; Reilly, A. C.; Holloway, B. C. Experimental Comparison of N(1s) X-Ray Photoelectron Spectroscopy Binding Energies of Hard and Elastic Amorphous Carbon Nitride Films with Reference Organic Compounds. *Carbon* **2003**, *41*, 1917–1923.

(39) Tan, X.; Fan, Q.; Wang, X.; Grambow, B. Eu(III) Sorption to TiO_2 (Anatase and Rutile): Batch, XPS, and EXAFS Studies. *Environ. Sci. Technol.* **2009**, *43*, 3115–3121.

(40) Liu, J.; Tao, R.; Guo, Z.; Regalbuto, J. R.; Marshall, C. L.; Klie, R. F.; Miller, J. T.; Meyer, R. J. Selective Adsorption of Manganese onto Rhodium for Optimized $Mn/Rh/SiO_2$ Alcohol Synthesis Catalysts. *ChemCatChem* **2013**, *5*, 3665–3672.

(41) Mahmoodi, S.; Ehsani, M. R.; Ghoreishi, S. M. Effect of Promoter in the Oxidative Coupling of Methane over Synthesized Mn/SiO_2 Nanocatalysts via Incipient Wetness Impregnation. *J. Ind. Eng. Chem.* **2010**, *16*, 923–928.

(42) Ignacio-de Leon, P. A.; Ferrandon, M.; Savereide, L. M.; Nauert, S. L.; Moncada, J.; Klet, R.; Chapman, K.; Delferro, M.; Camacho-Bunquin, J.; Carrero, C. A.; Notestein, J. M.; Nguyen, S. Promoter Effects on Catalyst Selectivity and Stability for Propylene Partial Oxidation to Acrolein. *Catal Lett* **2020**, *150*, 826–836.

(43) Post, J. E.; McKeown, D. A.; Heaney, P. J. Raman Spectroscopy Study of Manganese Oxides: Tunnel Structures. *Am. Mineral.* **2020**, *105*, 1175–1190.

(44) Bernardini, S.; Bellatreccia, F.; Casanova Municchia, A.; Della Ventura, G.; Sodo, A. Raman Spectra of Natural Manganese Oxides. *J. Raman Spectrosc.* **2019**, *50*, 873–888.

(45) Kijlstra, W. S.; Poels, E. K.; Bliek, A.; Weckhuysen, B. M.; Schoonheydt, R. A. Characterization of Al_2O_3-Supported Manganese Oxides by Electron Spin Resonance and Diffuse Reflectance Spectroscopy. *J. Phys. Chem. B* **1997**, *101*, 309–316.

(46) Fulghum, J. E.; Linton, R. W. Quantitation of Coverages on Rough Surfaces by XPS: An Overview. *Surf. Interface Anal.* **1988**, *13*, 186–192.

(47) Feng, X.; Cox, D. F. Oxidation of MnO(100) and $NaMnO_2$ Formation: Characterization of Mn^{2+} and Mn^{3+} Surfaces via XPS and Water TPD. *Surface Science* **2018**, *675*, 47–53.

(48) Kundu, A. K.; Menon, K. S. R. Growth and Characterization of Ultrathin Epitaxial MnO Film on Ag(001). *J. Cryst. Growth* **2016**, *446*, 85–91.

(49) Tang, X.; Gao, F.; Xiang, Y.; Yi, H.; Zhao, S.; Liu, X.; Li, Y. Effect of Potassium-Precursor Promoters on Catalytic Oxidation Activity of Mn-CoO_x Catalysts for NO Removal. *Ind. Eng. Chem. Res.* **2015**, *54*, 9116–9123.

(50) Ilton, E. S.; Post, J. E.; Heaney, P. J.; Ling, F. T.; Kerisit, S. N. XPS Determination of Mn Oxidation States in Mn (Hydr)Oxides. *Appl. Surf. Sci.* **2016**, *366*, 475–485.

(51) Cerrato, J. M.; Hochella, M. F. Jr.; Knocke, W. R.; Dietrich, A. M.; Cromer, T. F. Use of XPS to Identify the Oxidation State of Mn in Solid Surfaces of Filtration Media Oxide Samples from Drinking Water Treatment Plants. *Environ. Sci. Technol.* **2010**, *44*, 5881–5886.

(52) Rodriguez-Gomez, A.; Chowdhury, A. D.; Caglayan, M.; Bau, J. A.; Abou-Hamad, E.; Gascon, J. Non-Oxidative Dehydrogenation of Isobutane over Supported Vanadium Oxide: Nature of the Active Sites and Coke Formation. *Catal. Sci. Technol.* **2020**, *10*, 6139–6151.

(53) Liu, Q.; Yang, Z.; Luo, M.; Zhao, Z.; Wang, J.; Xie, Z.; Guo, L. Vanadium-Containing Dendritic Mesoporous Silica Nanoparticles: Multifunctional Catalysts for the Oxidative and Non-Oxidative Dehydrogenation of Propane to Propylene. *Microporous and Mesoporous Mater.* **2019**, *282*, 133–145.

(54) Pauling, L. *The Nature of the Chemical Bond* [Online]; Cornell University Press: Ithaca, NY, 1960. https://www.cornellpress.cornell.edu/book/9780801403330/the-nature-of-the-chemical-bond/ (accessed 2024-05-14)

(55) Solsona, B.; Blasco, T.; López Nieto, J. M.; Peña, M. L.; Rey, F.; Vidal-Moya, A. Vanadium Oxide Supported on Mesoporous MCM-41 as Selective Catalysts in the Oxidative Dehydrogenation of Alkanes. *J. Catal.* **2001**, *203*, 443–452.

(56) Gao, F.; Zhang, Y.; Wan, H.; Kong, Y.; Wu, X.; Dong, L.; Li, B.; Chen, Y. The States of Vanadium Species in V-SBA-15 Synthesized under Different pH Values. *Microporous and Mesoporous Mater.* **2008**, *110*, 508–516.

(57) Rybarczyk, P.; Berndt, H.; Radnik, J.; Pohl, M.-M.; Buyevskaya, O.; Baerns, M.; Brückner, A. The Structure of Active Sites in *Me*–V–O Catalysts (*Me* = Mg, Zn, Pb) and Its Influence on the Catalytic Performance in the Oxidative Dehydrogenation (ODH) of Propane. *J. Catal.* **2001**, *202*, 45–58.

(58) Wang, H.; Zhou, H.; Li, S.; Ge, X.; Wang, L.; Jin, Z.; Wang, C.; Ma, J.; Chu, X.; Meng, X.; Zhang, W.; Xiao, F.-S. Strong Oxide–Support Interactions Accelerate Selective Dehydrogenation of Propane by Modulating the Surface Oxygen. *ACS Catal.* **2020**, *10*, 10559–10569.

(59) MacRae, C. M.; Wilson, N. C. Luminescence Database I—Minerals and Materials. *Microsc. Microanal.* **2008**, *14* (2), 184–204.

(60) Omri, K.; Alyamani, A.; Mir, L. E. Photoluminescence and Cathodoluminescence of Mn Doped Zinc Silicate Nanophosphors for Green and Yellow Field Emissions Displays. *Appl. Phys. A: Solids Surf.* **2018**, *124*, 215.

(61) Adachi, S. Mn^{4+} vs Mn^{2+}—A Comparative Study as Efficient Activator Ions in Phosphor Materials: A Review. *J. Lumin.* **2023**, *263*, 119993.

(62) Scheithauer, M.; Bosch, E.; Schubert, U. A.; Knözinger, H.; Cheung, T.-K.; Jentoft, F. C.; Gates, B. C.; Tesche, B. Spectroscopic and Microscopic Characterization of Iron- and/or Manganese-Promoted Sulfated Zirconia. *J. Catal.* **1998**, *177*, 137–146.

(63) Nandy, A.; Tiwary, C. S.; Dutta, A.; Chattopadhyay, K.; Pradhan, S. K. Effect of Manganese (II) Oxide on Microstructure and Ionic Transport Properties of Nanostructured Cubic Zirconia. *Electrochim. Acta* **2015**, *170*, 360–368.

(64) Valigi, M.; Gazzoli, D.; Dragone, R.; Marucci, A.; Mattei, G. Manganese Oxide–Zirconium Oxide Solid Solutions. An X-Ray Diffraction, Raman Spectroscopy, Thermogravimetry and Magnetic Study. *J. Mater. Chem.* **1996**, *6*, 403–408.

(65) Jentoft, F. C.; Hahn, A.; Kröhnert, J.; Lorenz, G.; Jentoft, R. E.; Ressler, T.; Wild, U.; Schlögl, R.; Häßner, C.; Köhler, K. Incorporation of Manganese and Iron into the Zirconia Lattice in Promoted Sulfated Zirconia Catalysts. *J. Catal. 224*, 124–137.

(66) Chastain, J.; King, Jr., R. C. *Handbook of X-Ray Photoelectron Spectroscopy*; Perkin-Elmer Corporation, 1992.

(67) Biju, V.; Abdul Khadar, M. Electronic Structure of Nanostructured Nickel Oxide Using Ni 2p XPS Analysis. *J. Nanopart. Res.* **2002**, *4*, 247–253.

(68) Kwon, D. H.; Lee, S. R.; Choi, Y. S.; Son, S. B.; Oh, K. H.; Char, K.; Kim, M. Observation of the Ni_2O_3 Phase in a NiO Thin-Film Resistive Switching System. *Phys. Status Solidi RRL* **2017**, *11* (5), 1700048.

(69) Alsabet, M.; Grden, M.; Jerkiewicz, G. Electrochemical Growth of Surface Oxides on Nickel. Part 2: Formation of β-$Ni(OH)_2$ and NiO in Relation to the Polarization Potential, Polarization Time, and Temperature. *Electrocatalysis* **2014**, *5*, 136–147.

(70) Renaudin, G.; Gomes, S.; Nedelec, J. M. First-Row Transition Metal Doping in Calcium Phosphate Bioceramics: A Detailed Crystallographic Study. *Materials* **2017**, *10*, 92.

(71) Ferrara, C.; Eames, C.; Saiful Islam, M.; Tealdi, C. Lattice Strain Effects on Doping, Hydration and Proton Transport in Scheelite-Type Electrolytes for Solid Oxide Fuel Cells. *Phys. Chem. Chem. Phys.* **2016**, *18*, 29330–29336.

(72) Bennett, N. S.; Radamson, H. H.; Beer, C. S.; Smith, A. J.; Gwilliam, R. M.; Cowern, N. E. B.; Sealy, B. J. Enhanced N-Type Dopant Solubility in Tensile-Strained Si. *Thin Solid Films* **2008**, *517*, 331–333.

(73) Zhu, J.; Liu, F.; Stringfellow, G. B.; Wei, S. H. Strain-Enhanced Doping in Semiconductors: Effects of Dopant Size and Charge State. *Phys. Rev. Lett.* **2010**, *105*, 195503.

(74) Sadigh, B.; Lenosky, T. J.; Caturla, M. J.; Quong, A. A.; Benedict, L. X.; Diaz De La Rubia, T.; Giles, M. M.; Foad, M.; Spataru, C. D.; Louie, S. G. Large Enhancement of Boron Solubility in Silicon Due to Biaxial Stress. *Appl. Phys. Lett.* **2002**, *80*, 4738–4740.

(75) Li, Z.; Hu, X.; Zhang, L.; Liu, S.; Lu, G. Steam Reforming of Acetic Acid over Ni/ZrO_2 Catalysts: Effects of Nickel Loading and Particle Size on Product Distribution and Coke Formation. *Appl. Catal., A* **2012**, *417–418*, 281–289.

(76) He, Y.; Yang, K. R.; Yu, Z.; Fishman, Z. S.; Achola, L. A.; Tobin, Z. M.; Heinlein, J. A.; Hu, S.; Suib, S. L.; Batista, V. S.; Pfefferle, L. D. Catalytic Manganese Oxide Nanostructures for the Reverse Water Gas Shift Reaction. *Nanoscale* **2019**, *11*, 16677–16688.

(77) Mark, L. O.; Dorn, R. W.; McDermott, W. P.; Agbi, T. O.; Altvater, N. R.; Jansen, J.; Lebrón-Rodríguez, E. A.; Cendejas, M. C.; Rossini, A. J.; Hermans, I. Highly Selective Carbon-Supported Boron for Oxidative Dehydrogenation of Propane. *ChemCatChem* **2021**, *13*, 3611–3618.

(78) Alasiri, H.; Ahmed, S.; Rahman, F.; Al-Amer, A.; Majeed, U. B. Synthesis, Characterization, and Evaluation of High Selectivity Mixed Molybdenum and Vanadium Oxide Catalysts for Oxidative Dehydrogenation of Propane. *Can. J. Chem. Eng.* **2019**, *97*, 2340–2346.

(79) Guo, X. P.; Wang, X. X.; Lu, H. Q.; Liu, Z. M. Mesoporous Sol–Gel Silica Supported Vanadium Oxide as Effective Catalysts in Oxidative Dehydrogenation of Propane to Propylene. *RSC Adv.* **2023**, *13*, 22815–22823.

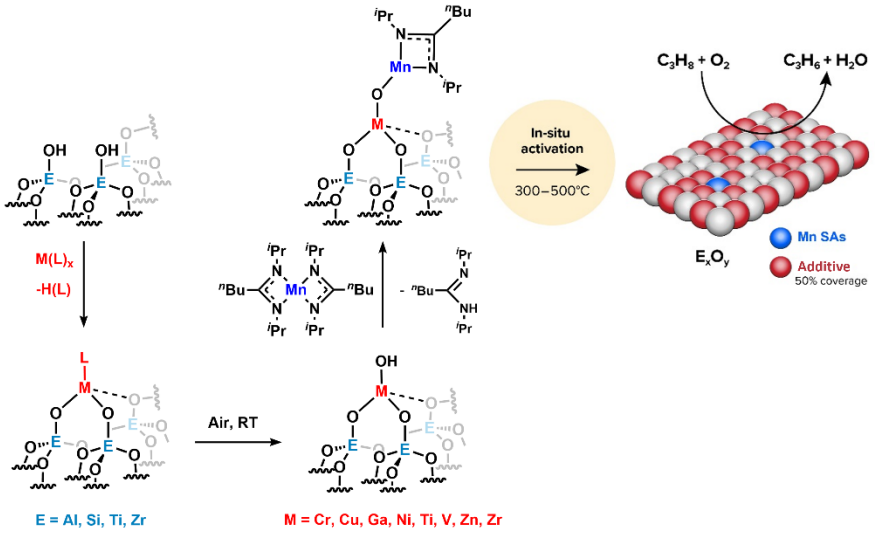

TOC